Deposition of hydroxyapatite coatings by axial plasma spraying: Influence of feedstock characteristics on coating microstructure, phase content and mechanical properties

Ashish Ganvir [c,*], Sainyam Nagar [b], Nicolaie Markocsan [a], Kantesh Balani [b]

[a] *University West, 46186 Trollhättan, Sweden*
[b] *Indian Institute of Technology, Kanpur, India*
[c] *University of Turku, Finland*

ABSTRACT

Axial plasma spray is one of the thermal spray techniques to deposit multifunctional advanced coatings. The present work explores the use of this process to deposit thin, continuous, and adherent $Ca_5(PO_4)_3OH$ (hydroxyapatite, HAp) coatings and characterize its microstructure, phases, hardness and adhesion strength. Three different suspension-deposited HAp coatings were investigated and compared with powder-deposited HAp coating on a Ti6Al4V substrate. The effect of mean solute particle size and solid-loading in the suspension has been explored on the evolution of microstructure, phase content and mechanical properties of axial suspension plasma sprayed (ASPS) coatings. Phase-characterization has shown retention of hydroxyapatite phase and coating crystallinity in the deposited coatings, whereas the adhesion strength of the HAp coating decreased from ~40 MPa to ~13 MPa when bioglass was added to the feedstock material. The lower solid load content and lower mean solute particle size in the suspension were found to be beneficial in achieving porous, rougher, and well-adhering coatings. This work concludes that ASPS can potentially deposit thin HAp coatings (< 50 µm) with high adhesion strength.

1. Introduction

Hydroxyapatite (HAp) is a bioceramic material that has Ca/P ratio close to that of natural bone i.e., < 1.67 owing to substitution of Ca ions by metabolic ions such as Mg, Na, K and others. Excellent osteo-conductive nature of HAp makes it an ideal candidate as a coating material in biomedical applications such as hip and dental implants [1]. HAp coatings have shown to provide an enhanced performance in dental implants [2], tibial components for total-knee- [3] and total-hip replacement arthroplasty [4]. Conventional thermal spray technique to deposit such bio coatings so far has been atmospheric plasma spraying (APS) where HAp ceramic powder is radially injected into the plasma plume where it gets melted and deposited on the surface of the implant to form a uniform coating [5–10]. APS is the most common thermal spray process for fabricating HAp coatings due to its relatively low cost and ability to coat large areas of complex shapes [5]. In fact, plasma spraying is the only thermal spray process which is approved by the FDA (Food and Drug Administration), USA, to be used for depositing HAp coatings as medical implants.

Ideal HAp coatings for orthopedic implants need to be thin (<50 µm) with high adhesion and strong cohesive strength so that it does not delaminate or crack under surface shear forces, high hardness so as to reduce the wear, and possess enough roughness as well as sufficient porosity to promote the ingrowth of bone tissues [1,5]. Moreover, high coating crystallinity (>45 %) [11] is also needed as the amorphous phase can undergo in-vivo dissolution under the human body fluid conditions [1]. However, a certain amount of amorphous phase is beneficial for osseointegration and for precipitation of secondary, bone-like HAp on contact with biofluid. The current trend in both research as well as the industrial practice is therefore to fabricate thin (<50 µm) HAp coatings while retaining the abovementioned characteristics [12,13]. However, the challenge with the thin coatings is that it tends to dissolve rapidly.

Achieving all the above mentioned properties along with the lower thickness is a challenge when using APS technique [13,14]. This is because the deposition of ceramic coating by APS implies a coating build

up by large splats that commensurate with the initial large feedstock powder particles inherent to the process (typically in the range of 10−100 s µm), which limits the deposition of lower coating thickness (<50 µm). Moreover, APS requires HAp powders with good flowabilty, and fine feedstock powders requires tedious agglomeration processes such as spray drying, fusing and crushing etc. [14]. In addition, APS-sprayed HAp coatings also showed poor performance due to low adhesion strength and phase degradation during spraying [5,15].

APS-sprayed HAp coatings are characterized by its lamellar structure full of porosity which is considered as advantageous for enhancing the in-growth of bone cells into HAp coatings [1,5]. However, other coating characteristics such as friction, wear, cohesive and adhesive strengths and corrosion resistance can decrease significantly with increasing porosity [16]. The denser the microstructure of the HAp coating, the lower is the risk of cohesive spallation due to cracking during *in vivo* contact with body fluids as well as the load-imposed mechanical strain on the implant [17]. These two conflicting requirements of porosity for obtaining enhanced bone cell in-growth and its absence for superior cohesion and adhesion strength puts stringent demands during coating deposition The porosity of about 1%–10% is typically observed in APS deposited HAp coatings [16,18–20] with the mean pore size in the range of about 300 µm [1]. For biomedical application, i.e., optimum ingrowth of bone cells, significantly higher porosities than 10 % are required.

Like the presence of porosity, coating surface roughness also plays a decisive role in the quest of enhancing the in-growth of bone cells in the bio ceramic coatings. Therefore, achieving an optimum surface roughness of plasma sprayed bio-ceramic coatings is also considered a crucial design factor [5]. The typical surface roughness (Ra) observed for the APS sprayed HAp coatings is in the range of 9−10 µm [5,21], however Heimann et al. [21] reported even higher roughness up to about 20 µm using APS.

More recently, suspension plasma spraying (SPS) is being studied widely as an alternate technique to conventional APS [13]. It was observed in some preliminary work that SPS can successfully deposit thin, porous and rough coatings [13,22]. This is attributed to utilizing suspension of fine ceramic powder particles (<5 µm) (in water or ethanol) allowing to deposit thin (<50 µm) coatings [23,24]. In addition to its ability to produce thinner coatings, SPS allows the deposition of coatings with submicrometer and nanometer length scale roughness due to the utilization of fine powder feedstock particles for thermal spraying [5]. Another advantage of using HAp suspensions over HAp powder is that it reduces the possibility of phase degradation of HAp during spraying since the suspended HAp material is "shielded" by a liquid droplet during the early stages of its in-flight journey. Hence, a significant amount of heat from the plasma is used to evaporate the solvent (water/ethanol) from the suspension which reduces the heat exchange between the HAp powder particles and plasma, thus, minimizing the phase degradation.

A recent development in the plasma spray technology is the advent of the high power axial plasma spray process, whereby the feedstock is axially injected in the plasma, i.e. parallel to the direction of the plasma jet [25,26], unlike in conventional radial plasma spray where the feedstock is injected perpendicular to the direction of the plasma. This high power axial plasma spray, especially axial suspension plasma spray (ASPS) has shown to be an extremely versatile technique, capable of producing a variety of interesting microstructures: such as highly dense, highly porous, vertically cracked, feathery etc. [27,28]. Moreover, the microstructures produced by ASPS have spanned a wide range of total porosity, from as low as 2–3 % [29] to beyond 40 % [28], as well as a wide pore size distribution, ranging from few nanometers to tens of micrometers [27,30]. So far, the ASPS process has been predominantly studied for deposition of Thermal Barrier Coatings (TBCs) used in gas turbine applications. However, due to its versatility, exploring this technique for various other potential applications including biocoating, as reported in this work, is worthwhile. Although, axial injection has been, so far, used mostly for depositing materials with high melting

points and with high decomposition stability such as zirconia or alumina, the approach is very useful while depositing liquid feedstock such as suspension or solution precursor of even low melting point and thermally-decomposing materials such as hydroxyapatite. A significant amount of energy is consumed from the hot plasma in evaporating the solvent from the suspension while processing suspension feedstock via ASPS. This means that an extra power and enthalpy are required when compared to that of processing of powder feedstock alone. Therefore, its processing demands the presence of suspension droplets within the hot zone for a longer duration, which is possible if axial injection approach is utilized as realized in ASPS as opposed to the traditional radial injection approach.

This preliminary work is an attempt towards exploring axial plasma spray technology to deposit thin and homogeneous HAp coatings on titanium alloy Ti-6Al-4 V substrate. The coatings were characterized using scanning electron microscopy, X-ray diffraction and tested for their hardness and adhesion strength. The effect of feedstock characteristics on various coating attributes was of specific interest.

2. Materials and methods

2.1. Feedstock preparation and coating deposition

The details of feedstock characteristics are provided in Table 1. For the reference APS coating, a commercially available HAp powder (Captal 30 SD, Plasma Biotal Ltd, Derbyshire, England) was used whereas for the ASPS coating deposition, two commercially available suspensions i.e., Suspension-B and Suspension-C (Colorobbia consulting S.r.l., Florence, Italy) were used. The Suspension-C contained 45S5 bioglass, with chemical composition (in weight %) 45.0 % SiO_2, 6.0 % P_2O_5, 24.5 % CaO, 24.5 % Na_2O. In addition, a lab-made Suspension-A was also used prepared by mechanically mixing a commercially available HAp powder (Medipure, Medicoat France, Etupes, France) with a bimodal size distribution (30 vol.% with d_{50} of 680 µm and 70 vol.% with d_{50} of 4.7 µm) in distilled water. All suspensions were kept agitated for 48 h to avoid any sedimentation of suspensions prior to spraying. The solid load was measured as the ratio of the leftover powder after drying a 100 mL suspension at 150 °C for 4 h and the initial suspension weight.

All four feedstocks were sprayed using an Axial III high power plasma torch (Northwest Mettech Corp., Vancouver, Canada) on identical Ti6Al4V coupon substrates of dimension (ϕ25 mm x 6 mm). G4™ Gravimetric Powder Feeder (Uniquecoat Technologies, LLC, Oilville, USA) and Nanofeed 350 suspension feed system (Northwest Mettech Corp., Vancouver, Canada) were used for feeding powder and suspension feedstocks, respectively. The process parameters used are summarized in Table 2. Although the same plasma torch was used to spray powder, the spray parameters utilized were different than used for the suspension feedstocks. The selection of the process parameters was based on the suggestions provided by the torch manufacturer as well as the authors of earlier work on HAp coatings [31]. All suspension feedstocks were sprayed under identical spraying conditions to ensure that any variations in microstructure are attributable only to variations in suspension properties. Prior to spraying, the substrates were grit blasted to a roughness of approximately R_a of 3 µm using alumina grit (63 ± 10 µm) at an air pressure of 5.5 bars. The number of plasma torch passes used to deposit different feedstocks were respectively 4, 10, 10 and 6 for powder, Suspension-A, Suspension-B and Suspension-C.

2.2. Feedstock and coating characterization

Both feedstocks as well as their respective coatings on Ti6Al4V substrates were analyzed for phase identification using X-ray powder 2000D diffractometer (Seifert, Mannheim, Germany), at 25 kV and 15 mA, using Cu-Kα (λ =1.541 Å) radiation at a scan rate of 0.5°/min, and a step size of 0.02°. Phase identification and the quantification of the identified phases by Rietveld analysis were performed using HighScore

Table 1
Characteristics of different feedstocks used in this study.

Suspension ID	Solvent	Solute	Solid load (wt. %)	Mean solute particle size (μm)	Solute morphology	Solute preparation
Suspension-A	Water	HAp	23	4−5	Irregular	Lab-made
Suspension-B	Water	HAp	13	0.3−0.6	Regular (Agglomerated)	Commercial
Suspension-C	Water	HAp + Bioglass (80−20 wt. %)	27	0.3−0.6	Regular (Agglomerated)	Commercial
Powder	–	HAp	–	30−40	Regular (Spherical)	Commercial

Table 2
Plasma spray parameters used to deposit powder and suspension feedstocks.

Feedstock/Spray parameters	Powder feed rate (g/min)	Suspension feed rate (ml/min)	Current (A)	Spray distance (mm)	Plasma gas composition (%)			Total Gas Flow (l/min)	Carrier Gas flow (slpm)	Power (kW)	Enthalpy (kJ)
					Ar	H$_2$	N$_2$				
Powder feedstock (APS)	11	NA	230	150	0	20	80	150	30	114	17
Suspension feedstock (ASPS)	n.a.	45	220	70	70	20	10	200	5	89	7

Plus software [32].

The relative coating crystallinity was determined by Rutland method from the XRD patterns of feedstocks and the corresponding coating using the following equation [33–35]:

$$Coating\ crystallinity\ (\%) = \frac{\Sigma A_C}{(\Sigma A_C + \Sigma A_A)} \times 100 \qquad (1)$$

where ΣA_C is the sum of the area under all the peaks of crystalline HAp feedstock, and ΣA_A is the sum of the area under all amorphous humps of HAp coating. The peak-area of the feedstocks and the coatings were calculated between diffraction angles 2θ from 20° to 61°. The total area under all XRD peaks was calculated by summing-up the area of small rectangles of length $((Y2 + Y1)/2)$ and width $(X2-X1)$ where Y1, Y2 and X1, X2 are the two consecutive data points on y-axis and x-axis for peak intensity and 2θ, respectively, for each coating and their respective feedstock powders.

The surface roughness of the coating was measured using a MITU-TOYO SURFTEST-301 (Mituyoto, Takatsu-ku, Kawasaki, Japan) profilometer. Microstructure and morphology of both feedstocks and coatings were analyzed using HITACHI TM3000 (Tokyo, Japan) and EVO 50 (ZEISS, Oberkochen, Germany) scanning electron microscopes (SEMs).

All coatings were metallographically prepared for microstructural analysis. The samples were first mounted in a low viscosity epoxy resin 301 (Logitech Ltd., Glasgow, UK) using vacuum impregnation technique. Cross sections were cut using an alumina cut-off wheel (Struers 50A20) at 1600 rpm with 0.03 mm/s feed rate and re-mounted again in a fast-curing EpoxiCure resin (Buehler, Lake Bluff, Illinois, USA) using vacuum impregnation technique. The double mounted samples were ground and mirror polished semi-automatically using a Buehler PowerPro 5000 (Buehler, Lake Bluff, Illinois, USA) machine. Porosity was measured using a public domain Java based image processing program (Fiji) ImageJ software [36]. SEM images in backscattered mode were captured and converted into binary by appropriately adjusting the grey scale threshold. Relative area fraction of white region (porosity) compared to the black region (material) was calculated using the ImageJ software. The average of ten different SEM micrographs was finally reported with appropriate standard deviation. More details about image analysis technique for thermally sprayed coatings can be found elsewhere [37].

2.3. Hardness and adhesion strength measurement

The hardness of the coatings was measured using a Vickers indenter (Shimadzu HMV-2 T Microhardness Tester) on polished cross-sectioned samples. A total of ten indents were made across the coating cross-

section at a maximum load of 245 mN for 10 s. To measure the adhesion strength of the coatings, Standard Tensile Adhesion Test (EN-582, ASTM-C633) was carried out [24]. According to this standard test, a test specimen of 25 mm diameter was joined with the top and bottom counter parts using an adhesive agent (FM® 1000 epoxy glue, Cytec Industries Inc. NJ, USA). The whole glued specimen along with the counter parts were cured for about 90 min about 170 °C. The tensile load was, then, gradually applied using a universal MTS Criterion Model 45 (MTS Systems SAS, Creteil, France) tensile testing machine at a crosshead speed of 1.27 mm/min. The adhesion strength was calculated as the ratio between the load at which the rupture occurred and the coating surface area. All the coatings showed failure in the HAp coating after the adhesion testing except coating ASPS-B which showed a failure at the epoxy glue-HAp coating interface. To obtain statistically relevant data, three samples for each coating type were tested and the mean value with their respective standard deviation is reported.

3. Results and discussion

3.1. Feedstock characteristics

The morphology and the size distribution of particles of the feedstocks were analyzed in SEM. As illustrated in Fig. 1, the powder used for depositing APS coatings (Fig. 1 (a)) had a uniform spherical shape with a particle size distribution within a range of few tens of micrometers, confirming the range provided by the manufacturer (see Table 1). On the contrary, the shape of the powder particles used to prepare Suspension-A (Fig. 1(b)) was slightly irregular with the presence of micrometric powders (i.e., the particle size in the range of few micrometers) as also suggested by the manufacturer (see Table 1). Similarly, both commercial Suspension-B as well as Suspension-C showed irregular particle shapes (Fig. 1 (c) and (d), respectively) as well as the presence of agglomerates of particles in the range of few hundreds of nanometers, as provided by the manufacturer (See Table 1).

In addition to the particle shape and the size range of powders in all suspensions, the solid loading was measured prior to the deposition of suspensions as reported in Table 1. Both commercially obtained suspensions (Suspension-B and Suspension-C) had a solid loading of 13 wt. % and 27 wt. %, respectively, whereas the lab made Suspension-A was 23 wt. % solid loaded. It should be noted that the Suspension-C contained bioglass of about 20 % of the total solid load by weight, which means about 5 wt. % of bioglass. Also, Suspension-C was apparently more viscous compared to the other suspensions used in this study, which could possibly be related to the presence of bioglass.
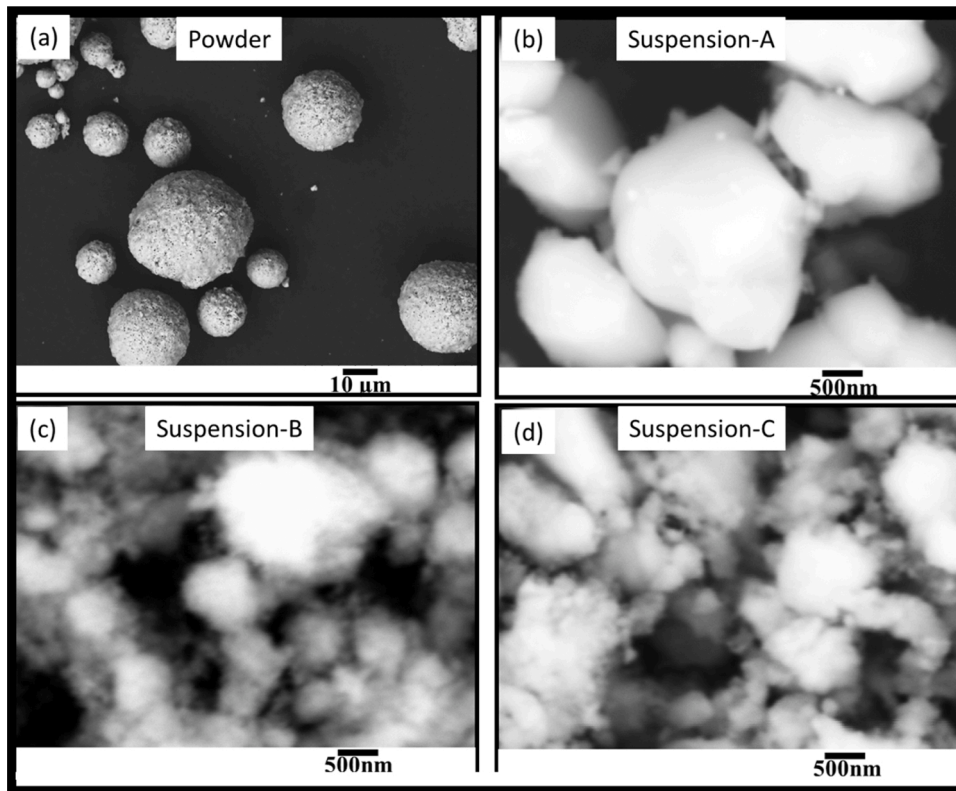
Fig. 1. Particle size and morphology of different HAp feedstocks i.e. (a) Powder, (b) Suspension-A, (c) Suspension-B and (d) Suspension-C.

3.2. Coating characteristics

3.2.1. Top-view and surface roughness

Fig. 2 shows the top-view of the as-sprayed coatings observed under SEM. Worthy to be mentioned here is the presence of nodular shaped features (as marked by white arrows) in case of ASPS-A and ASPS-B which are absent in both ASPS-C as well as APS coatings. The presence of these features is due to the shallow deposition of molten ceramic droplets resulting from the well-known shadowing effect and its consequent result on producing nodules around the substrate surface imperfections in ASPS coatings [38]. Subsequent shallow deposition of

low momentum droplets over the asperities due to the ensuing passage of the plasma torch leads to the shadow effect forming column-like or tree-like features around the asperities [38] which appear like nodules in the top view as shown in Fig. 2 and indicated by white arrows.

The reason for the highest number of nodular type features in ASPS-B (see Fig. 2 (c)) can be related to the presence of least solid loading along with lower mean solute particle size in Suspension-B. A lower solid load and lower mean solute particle size can result in lower suspension droplet size and hence lower droplet momentum [38]. Similarly, ASPS-A coating also shows the presence of such features.

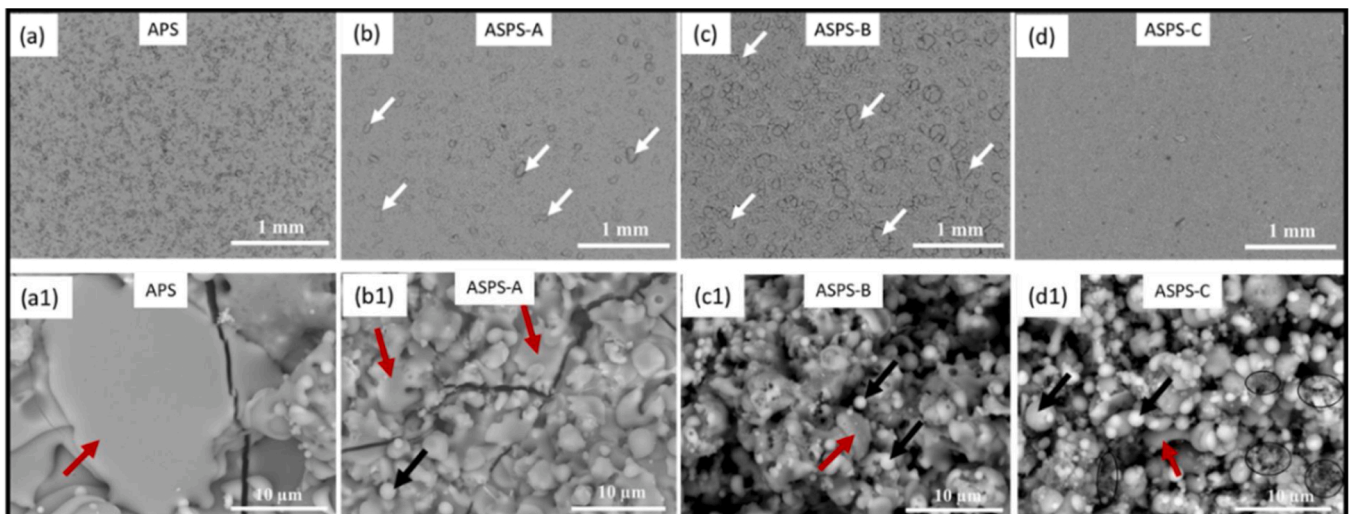The presence of such nodular features also results in rougher coating

Fig. 2. SEM images of the surfaces of the as-sprayed coatings ((a) APS, (b) ASPS-A, (c) ASPS-B and (d) ASPS-C) indicating the nodular type features (white arrows) and corresponding magnified SEM micrographs ((a1) APS, (b1) ASPS-A, (c1) ASPS-B and (d1) ASPS-C) of the top surface showing spherical particles (black arrows), splats (red arrows), non-molten region (black circles).

surface. As shown in Table 3, the surface roughness (Ra) of the ASPS-B coating was highest (7.6 μm) whereas ASPS-C coating showed the lowest (3.0 μm), which is well in agreement with the above observations of top surface microstructure. As mentioned earlier in the introduction section, surface roughness plays an important role in improving the in-growth of bone cells into the bioceramic coatings. Some studies have shown that the surface roughness of titanium implants in the range as depicted above is beneficial for enhanced osseointegration compared to the smooth implants [22]. In addition, the importance of nano-roughness (<100 nm) is also highlighted in the literature showing its positive effects on osteoblast adhesion and proliferation [5,23]. Fig. 2 (a1 to d1) shows the magnified SEM micrographs of the top surface of all coatings, affirming the presence of very fine spherical particles (marked by black arrows) as well as fine splats (marked by red arrows) in all the ASPS coatings (especially ASPS-B and ASPS-C coatings) that create fine scale roughness on the coating surface.

Significantly larger splat size (few tens of micrometer) in case of APS coating (Fig. 2 (a1)) compared to ASPS coatings is due to the original coarser feedstock (i.e., powder) particles used in case of APS. Similarly, comparing all the three ASPS coatings the ASPS-A coating showed significantly larger splats (in the range of about 5 μm–10 μm) than both ASPS-B and ASPS-C coatings. It should be noted that all the three ASPS coatings were deposited at the same plasma spray parameters and, therefore, the difference seen in Fig. 2 micrographs is solely due to the differences in the suspension properties. The larger splats in ASPS-A can be attributed to the higher solid loading and higher mean solute particle size of Suspension-A that makes atomization (breaking up the suspension stream into droplets) difficult. Thus, resulting in larger suspension droplets, which, in turn, form larger fully/partly molten ceramic droplets resulting in larger splats. On the contrary, ASPS-B had both significantly lower solid loading content as well as lower mean solute particle size resulting in an easy atomization and hence smaller suspension droplets and finer splats as evident from Fig. 2 (c1) with approximate average splat size of about 3 μm–5 μm along with few spherical particles of approximately less than 1.5 μm size.

The suspension droplets in case of Suspension-C could have been finer than Suspension-A but still larger than Suspension-B. This is because of the lower mean solute particle size, the presence of bioglass which resulted in lower overall suspension density (as bioglass is lighter) and higher suspension viscosity of Suspension-C. Hence, the approximate splat size of 3 μm–8 μm along with the presence of spherical particles of approximately less than 3 μm were noted in ASPS-C which were larger than that of ASPS-B but smaller than that of ASPS-A. Although, the presence of number of spherical particles were noted to be much higher in ASPS-C compared to ASPS-B coating (see Fig. 2(c1 and d1)). Additionally, ASPS-C coating also showed the presence of non-molten regions (as marked by black circles in Fig. 2(d1)). These non-molten regions can also be related to the higher solid loading and slightly viscous Suspension-C. This together could have resulted in a large enough suspension droplet size after atomization where most of the plasma heat could have been consumed in evaporating the solvent and agglomerating the solute particles. This means, eventually, some of the solute particles in the suspension droplet could not have been affected at all as shown schematically in Fig. 6. These non-affected solute particles could have eventually arrived at the substrate in their initial state as in

Suspension-C (see Fig. 1 (d)).

The typical shape of splats in plasma-sprayed coatings is known as pancake- or disc-like [39]. This was also observed in all the coatings studied in this work (see Fig. 2). However, not all the splats were like the typical pancake or disc shape, especially in case of ASPS coatings where some of the splats appeared as spherical shape (marked with black arrows in Fig. 2). These uniform spherical shape particles are also reported in the literature for ASPS deposited coatings [37]. In case of both ASPS-B and ASPS-C coatings, unlike that of ASPS-A, the presence of spherical particles was seen to be relatively higher, especially in ASPS-C. In case of both APS as well as ASPS-A coatings, bigger molten ceramic droplets formed due to the coarser initial powder size and coarser suspension droplet size, respectively, can travel through the core of the plasma before impacting the substrate for a significant duration of their in-flight journey. Moreover, due to their higher molten ceramic droplet mass, the droplets may not cool down as fast as the fine molten ceramic droplets as in the case of ASPS-B. Coarser ceramic molten droplets, as in case of ASPS-A and APS, can, therefore, arrive hot under fully/partly molten conditions at the substrate which upon impact form proper pancake shape splats. Whereas in case of ASPS-B and ASPS-C coatings, fine molten ceramic droplets may re-solidify to form re-solidified spherical particles in flight before impacting the substrate and arrive cold under re-solidified condition at the substrate. It must be noted that unlike conventional radial injection, axial injection of feedstock materials (either suspension/powder) will lead to better heat transfer from the plasma plume to the feedstock as they are introduced in the core of the plasma [39]. Especially, in case of high-power plasma torches such as Axial III Mettech coupled with feeding very fine size solute particles where it is unlikely to have many un-molten or even partially molten particles arriving at the substrate. This is also the reason that in all the coatings studied in this work, it is predominantly a combination of splats and re-solidified particles with the presence of some degree of non-molten region (only in ASPS-C).

3.2.2. Coating thickness

The cross-sections of all coatings captured in SEM at lower magnification are shown in Fig. 3. A thin and uniform coating can be seen in Fig. 3 (a–d) using both powder as well as suspension feedstocks. APS deposited coating was thickest among all followed by ASPS-C and ASPS-A with ASPS-B coating being the thinnest. However, a large standard deviation among all ASPS coating thicknesses suggests a statistical variation effect rather than a true influence of feedstock parameters on thickness. The thickness of all four coatings was quantified and are shown in Table 3. All three ASPS coatings were measured to be less than 50 μm in thickness that is reported to be beneficial for enhancing the adhesion strengths [5], as also discussed in later section. Among all ASPS coatings, both ASPS-A and ASPS-B coatings showed lower thickness. The deviation in thickness in ASPS-B can be related to the formation of several bumpy features (cross-sections of the nodules as observed in top surface) giving a significant variation in thickness across cross-section.

Another observation to be pointed out here is the thickness per pass (μm/pass) which is 18, 4, 4 and 8 μm/pass for APS, ASPS-A, ASPS-B and ASPS-C coatings, respectively, as reported in Table 3. Significantly higher thickness per pass in case of APS coating can be related to the

Table 3

Various attributes of different HAp coatings (surface roughness, coating thickness, thickness per pass, porosity, crystallinity, hardness and adhesion strength).

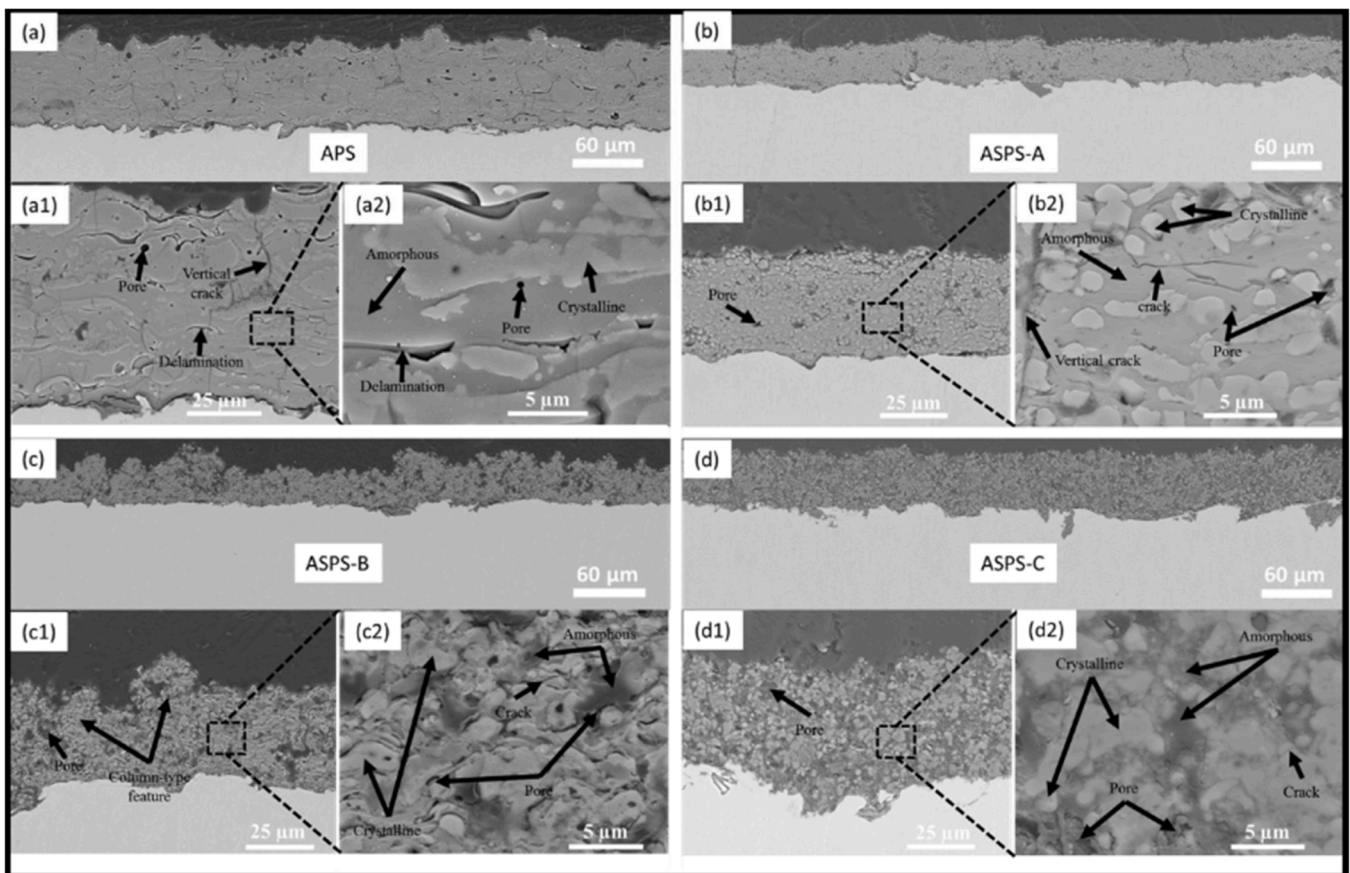| Coating ID/ Properties	Surface roughness (Ra) (μm)	Coating thickness (μm)	Coating thickness per pass (μm/pass)	Coating porosity (Area %)	Coating crystallinity (%)	Coating hardness (HV)	Coating adhesion strength (MPa)
APS	4.8 ± 0.7	71.0 ± 6.0	18	8.5 ± 0.9	66	334 ± 20	29 ± 3
ASPS-A	4.0 ± 0.8	39.5 ± 3.0	4	6.0 ± 1.7	43	324 ± 19	30 ± 4
ASPS-B	7.6 ± 0.9	38.5 ± 10.0	4	20.9 ± 5.6	40	87 ± 13	42 ± 10
ASPS-C	3.0 ± 0.5	49.5 ± 5.7	8	14.5 ± 6.4	37	89 ± 20	15 ± 3

Fig. 3. Polished cross-section SEM micrographs of different HAp coatings deposited using atmospheric plasma spraying: (a) APS, (b) ASPS-A, (c) ASPS-B and (d) ASPS-C at low magnification, (a1-d1) high magnification, and (a2-d2) higher magnifications.

presence of more material in the powder feedstock compared to in the suspension feedstocks where more than half of the total feedstock (by weight) was only solvent (water). In case of many thick coating applications such as TBCs, higher thickness per pass can be very attractive for industries. However, higher thickness per pass such as observed in this study for APS (i.e., 18 μm/pass) could be a limitation when there is a need to produce a very thin coating. This was one of the reasons to introduce and develop SPS. Therefore, ASPS is certainly a very attractive technology to produce such thinner coatings. As presented in this work, the lowest thickness per pass achieved was only about 4 μm/pass, which makes it possible to deposit a coating as thin as few micrometers if the ASPS process conditions are optimized accordingly.

The microstructure of all coatings was further analyzed in SEM at higher magnifications to get a closer look at their different microstructural features, which is shown in Fig. 3 (a1-d1) (at high magnification) and Fig. 3 (a2-d2) (at higher magnification). The quantification of the total porosity in all coatings is reported in Table 3. APS coatings as observed in Fig. 3 (a, a1 and a2) showed typical lamellar structure with the presence of delaminations, pores and vertical and horizontal cracks. On the contrary, ASPS sprayed coatings showed fine structured features such as fine pores and cracks with no delaminations, which is attributed to relatively finer solute powder particles used during spraying in ASPS compared to that in APS coating. Moreover, all the coatings have also shown the presence of light grey grains embedded in a relatively dark grey matrix, which, as reported in the literature [33,40], are crystalline and amorphous phases present in the plasma sprayed HAp coatings, respectively (see Fig. 3 (a2-d2)).

3.3. Phase analysis using XRD

XRD pattern of all coatings and their respective feedstocks are presented in Fig. 4. The quantification of the various phases presents in different feedstocks as well as their respective coatings are shown in Fig. 5(a) and (b), respectively. The powder as well as Suspension-A and Suspension-B feedstocks showed the presence of 100 % hydroxyapatite phase whereas Suspension-C in addition to the hydroxyapatite also showed the presence of bioglass (about 18 %). The presence of bioglass confirms the phase distribution as suggested by the manufacturer. However, it is more sensitive to heat exposure during spraying because the amount of remaining bioglass in the as-sprayed coating was slightly reduced (about 17 %) as compared to the feedstock. One of the major challenges of plasma spraying hydroxyapatite coatings on implants is the degradation of initial phases due to extremely high heat exposure during deposition process. Therefore, the requirement from FDA is to retain at least 80 % of the hydroxyapatite phase in the coatings after plasma spraying.

Other phases apart from HAp observed in the as-sprayed coatings studied in this work were $Ca_3O_8P_2$ or TCP, CaO, $Ca(OH)_2$ and $CaCO_3$. Such phases were also reported in literature in plasma-sprayed HAp coatings [5,40,41]. In addition to the phase content, the relative coating crystallinity determined, Table 3, shows showing highest value for the APS (66 %) followed by ASPS-A (43 %), ASPS-B (40 %) and ASPS-C (37 %). The minimum requirement as per ISO13779−2 [11] for the coating crystallinity in the plasma-sprayed HAp coatings is 45 %.

3.3.1. Phase degradation in plasma-sprayed HAp coatings

The intricate thermal history of the feedstock in the plasma plume and its complex solidification behavior presents unique challenges in
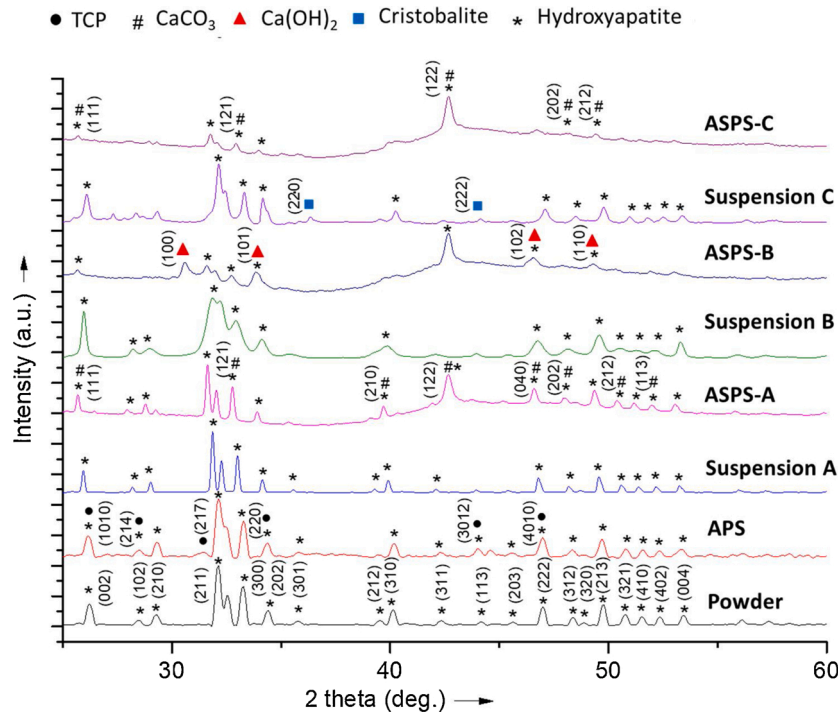
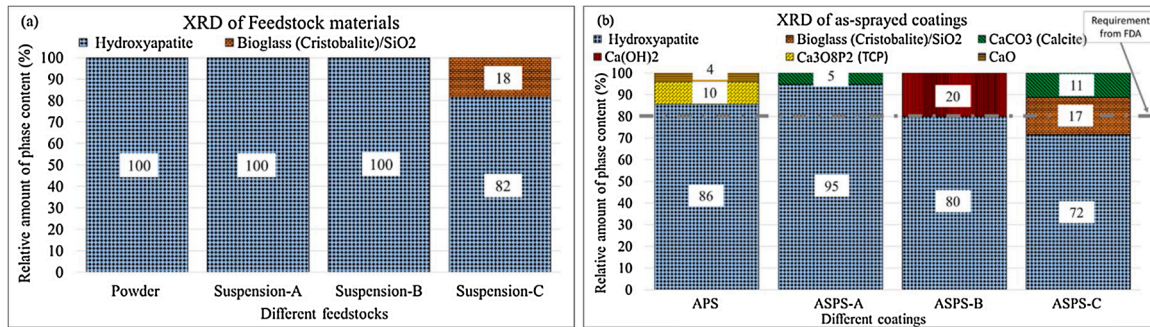**Fig. 4.** XRD patterns of all coatings and respective feedstocks showing various phases.
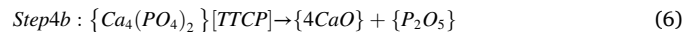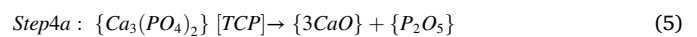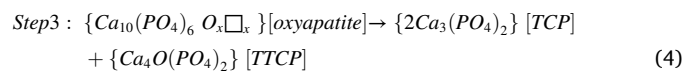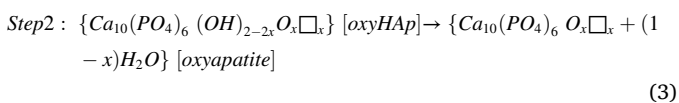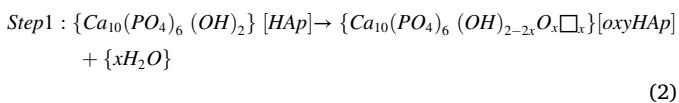

Fig. 5. Quantification done by Rietveld analysis of various XRD phases present in (a) different feedstock materials and in (b) their respective as-sprayed coatings.

understanding the exact phase transformation in plasma sprayed HAp coatings. The challenges aggravate even further as the nature of the feedstock changes from conventional solid powder to suspension. Nevertheless, simplistic theories have been discussed in literature regarding conventional radially injected powder feedstock plasma sprayed HAp coatings [42–44]. Heimann [5] proposed a four-step sequence thermal decomposition of conventional radially injected powder APS sprayed HAp coating. Here typically the HAp powder particle experiences extremely high temperatures in the hot zone of the plasma jet (>15,000 °C) for a very short residence time (~100 s of μs to few ms) and decomposes via incongruent melting in-flight as per the following sequence shown from Eq. (2) to (6) [5]:

$$Step1: \{Ca_{10}(PO_4)_6\,(OH)_2\}\,[HAp] \rightarrow \{Ca_{10}(PO_4)_6\,(OH)_{2-2x}O_x\square_x\}\,[oxyHAp]$$
$$+ \{xH_2O\} \tag{2}$$

$$Step2: \{Ca_{10}(PO_4)_6\,(OH)_{2-2x}O_x\square_x\}\,[oxyHAp] \rightarrow \{Ca_{10}(PO_4)_6\,O_x\square_x + (1-x)H_2O\}\,[oxyapatite] \tag{3}$$

$$Step3: \{Ca_{10}(PO_4)_6\,O_x\square_x\}\,[oxyapatite] \rightarrow \{2Ca_3(PO_4)_2\}\,[TCP]$$
$$+ \{Ca_4O(PO_4)_2\}\,[TTCP] \tag{4}$$

$$Step4a: \{Ca_3(PO_4)_2\}\,[TCP] \rightarrow \{3CaO\} + \{P_2O_5\} \tag{5}$$

$$Step4b: \{Ca_4(PO_4)_2\}\,[TTCP] \rightarrow \{4CaO\} + \{P_2O_5\} \tag{6}$$

In contrast to the conventional APS, where powder is fed into the plasma radially, in this study the APS sprayed coatings were deposited using axial injection approach. Although, there exists such a difference ('axial' vs 'radial') the sequence is assumed to be true for APS as well as ASPS sprayed coatings studied in this work. This is because the material (HAp) and the heating/melting source (plasma) are still the same. Nevertheless, the key difference between coating sprayed via ASPS (compared to APS), apart from the physical state of the feedstock (i.e., suspension instead of powder), is process parameters (see Table 2). Based on the above sequence, the outlined differences in 'conventional radial APS vs axial APS vs ASPS' and other available relevant literature on the suggested phase transformation models in conventional plasma sprayed HAp coatings [5,42–45], a simplified theoretical framework for the phase degradation in axial APS and ASPS deposited HAp coatings are

proposed and discussed below.

3.3.2. Phase degradation in axial APS sprayed HAp coating

During axial injection the powder particles experience uniform and homogeneous thermal history during their in-flight journey as all of it is injected in the core of the plasma compared to that of the radial injection approach (see Fig. 6). Thus, analyzing the thermal history of any powder particle during axial APS can be considered as a good representative of most of the powder particles unlike in conventional radial APS. Therefore, Fig. 6 schematically outlines various possible thermal decomposition scenarios of a given powder particle during axial APS. These scenarios are when the powder particle is under partially molten with solid-solid phase transformation (I), fully molten (II) and partially molten without solid-solid phase transformation (III) condition. Additionally, three more scenarios are possible (i.e., IA, IIA and IIIA) when the outer surface of the particle under the first three scenarios starts vaporizing (see Fig. 6 where scenario (IA) is shown as an example for its corresponding scenario (I)). Under each scenario the powder particle can have several regions as shown in Fig. 6 for scenario (IA) such as (a) a solid region (black) consisting of the original solid crystalline HAp, which is not affected by the plasma heat at all, (b) an another solid region (grey) but formed due to the solid-solid phase transition of pure crystalline hexagonal HAp into TTCP or TCP [43], (c) a liquid region (light grey), which is a melt consisting of several HAp phases such as pure crystalline hexagonal HAp, TTCP and TCP due to the solid-liquid phase transformation [5], and (d) a vapor region (white with black dots), which forms when the plasma plume temperature is higher than the surface temperature of the partially molten particle where the evaporation of P_2O_5 occurs resulting in the formation of CaO at the outer surface [43]. Each region can consist of one or more different phases in different proportions depending on particles' rate of thermal decomposition.

Different scenarios (as discussed above) can result in development of different type of splats, for example, IA* instead of IA and likewise as shown in Fig. 6 depending on particles' in-flight thermal decomposition scenario, rate of thermal decomposition and cooling rate during solidification. It should be noted that the representative spherical geometry shown under 'deposited particles after solidification' for these splats in Fig. 6 is just an over-simplification of the reality. Here, on impact, the orderly arrangement of the individual spherical shells can be lost, and the splat shape can be more like a pancake/disc. More profound analysis of the sequence of events occurring during deposition of a supersonically accelerated semi-molten HAp particle impinging on a roughened titanium alloy substrate is shown in literature [46], whereas, more specifically, the evolution of bio coatings during SPS has also been elucidated in literature [47]. Each of these splats can consist of one or more of any of the three regions in different proportions as shown in Fig. 6 for splat IA* i.e. (a) a solid region (black) formed due to the original crystalline region arriving at the substrate in its original state, (b) a solid region (grey) formed due to the solid-solid phase transition and arriving on the substrate in its decomposed state, and (c) a re-solidified region (dark grey) formed due to the re-solidification of the liquid region (light grey), which can be one or more of any of the amorphous HAp, TCP, TTCP, CaO or other Ca containing phases depending on the thermal decomposition rate and the cooling rate during solidification.

High cooling rate and decomposition content, which are typically observed at high plasma enthalpies, lead to the formation of a large amount of TCP, TTCP and amorphous HAp in the splat with subsequent decomposition of TTCP into CaO and P_2O_5 and recrystallization of only TCP as it completely dissolves in the melt [5,44]. On the contrary, lower cooling rate and decomposition content, as achieved under lower plasma enthalpies, lead to significantly reduced amount of TCP, TTCP and amorphous HAp in a splat. Hereupon, cooling the partially molten particle results in some re-crystallized TCP and TTCP along with mostly original crystalline HAp. As the plasma torch utilized in this study is a high power Mettech axial III torch and the used plasma power and enthalpy to deposit APS coating was 114 kW and 17 kJ, which is about two-threefold higher than the conventional powder radial APS sprayed HAp coatings [48], it can be assumed that the axial APS processing conditions in this study are directed towards the higher decomposition of HAp powder particles.

The presence of very high HAp phase content i.e., 86 % in the axial APS coating (see Fig. 5 (b)) suggests that most of the powder particles have either arrived at the substrate without getting significantly affected
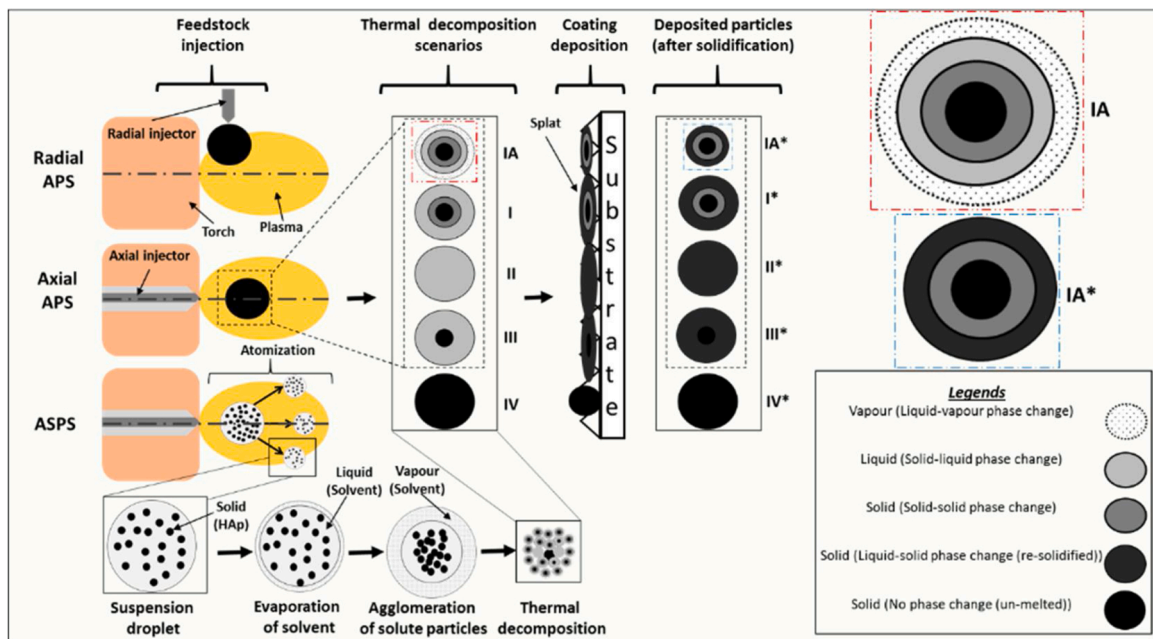

Fig. 6. Schematic of the in-flight thermal decomposition of HAp during plasma spraying of powder and suspension feedstock via axial injection and subsequent splat formation after solidification (*Note 1: Scenarios IIA and IIIA are not shown but can be imagined to be present similar to IA with an additional outer vapor region surrounding II and III for IIA and IIIA resulting in IIA* and IIIA* type of splats respectively. Note 2: The relative proportions of different regions shown by varied shading using several legends is not proportional to the respective shade areas in the legend and different regions can exist in different proportions in each scenario*).

(i.e. getting affected only at the outer surface and not in the core of the particle) by the plasma heat during its in-flight journey or underwent re-crystallization to HAp during solidification. The latter case is rather difficult in plasma spray process due to the higher cooling rates making it difficult for the recrystallization to occur suggesting that prior case could have most likely occurred in the axial APS coating studied in this work. This means that most of the particles might have followed any one or more of the scenarios (I, IA, III or IIIA), which can be further deduced from the reduced coating crystallinity of about 66 % from its original >95 % pure crystalline powder. Thus, relatively large portion (about 34 %) of any given powder particle was partially melted during the in-flight thermal decomposition and then re-solidified to form amorphous HAp. Additionally, the absence of TTCP suggests that there was no solid-solid phase transition suggesting the most likely scenarios were only III or IIIA. It should be noted that weak resolution of XRD might not have been able to detect TTCP and it might be present in minimal amounts in the coatings. Therefore, it can be said that about half of each of most of the particles (core) was unaffected by the plasma heat. Whereas the other half (outer region) was incongruently melted to a liquid which transformed to TTCP and subsequently decomposed into 4% CaO in-flight due to the vaporization of P_2O_5. In addition to that, about 10 % TCP was also re-crystallized along with about 34 % amorphous phase content as calculated by the Rutland method using Eq. 1 from the liquid melt during solidification. Such result is also substantiated from the cross-section SEM micrographs of the APS coating, where discrete light grey color grains of crystalline HAp/ TCP can be seen embedded in a continuous glassy dark grey amorphous phase matrix (see Fig. 3 (a2)).

3.3.3. Phase degradation in ASPS sprayed HAp coatings

Like axial APS, all the ASPS coatings also experienced phase degradation (see Fig. 5). As shown in Fig. 5 (b), in APS coating apart from HAp the two other major phases formed were TCP and CaO; whereas, in all ASPS coatings apart from HAp neither of these two phases were noticed, instead several other Ca containing phases were noticed. One of the possible reasons for such a difference can be attributed to the nature of the feedstock i.e., water-based suspension in ASPS vs powder in APS. Since CaO can easily transform into other Ca containing phases in the presence of water and CO_2 [5]. So, the proposed modified thermal decomposition sequence in case of ASPS coatings, in addition to the first

four steps as mentioned earlier for APS, can be as follows:

$$Step5 : CaO + H_2O \rightarrow Ca(OH)_2 \tag{7}$$

$$Step6 : Ca(OH)_2 + CO_2 \rightarrow CaCO_3 + H_2O \tag{8}$$
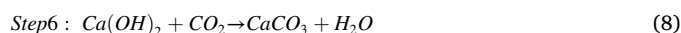
The exact cause of the presence of carbon is not yet very clear and requires further investigation. However, one of the possible explanations could be the presence of residues from the ethanol-based suspensions as the authors group uses the same suspension feeding setup, injector and plasma torch to deposit both water based as well as ethanol based suspensions for various applications. Another possible explanation could also be the introduction of other types of impurities while handling the HAp suspensions in the lab or the presence of atmospheric CO_2.

Unlike in APS, where the HAp feedstock was 'powder', but in ASPS it was 'suspension' consisting of very fine HAp solute powder particles suspended in a solvent (water) as shown in Fig. 6. Therefore, the differences in the phase degradation of all three ASPS-deposited coatings can be attributed to the suspension droplet size after atomization (see Fig. 6) instead of solely to the initial powder particle size as in APS. A large portion of the plasma heat is consumed in solvent (water) evaporation and agglomeration/sintering of fine HAp solute particles (see Fig. 6) prior to the phase degradation of a HAp solute particle in the suspension droplet via any of the six scenarios described for a powder particle in APS. In addition, an additional scenario (IV) in ASPS is also possible where an original pure crystalline fine HAp powder particle can arrive in its original form (phase, size, shape etc.) at the substrate without getting affected by the plasma heat at all and resulting in splat (IV*). As in ASPS, (a) a particle is protected by the liquid shell of the suspension droplet for a significant amount of time during its in-flight journey as shown in Fig. 6, (b) a significant amount of plasma heat is already consumed in evaporating the solvent and (c) the spray distance used in ASPS is typically very short (70 mm in this work) compared to the long spray distance in APS (150 mm in this work) reducing the residence time significantly. The amount of heat left for the phase degradation of the HAp solute particles in the suspension droplet depends on the solvent type and the atomized suspension droplet size. Since the solvent type was the same (i.e., water), the size of the atomized suspension droplet can be considered as the major factor deriving the
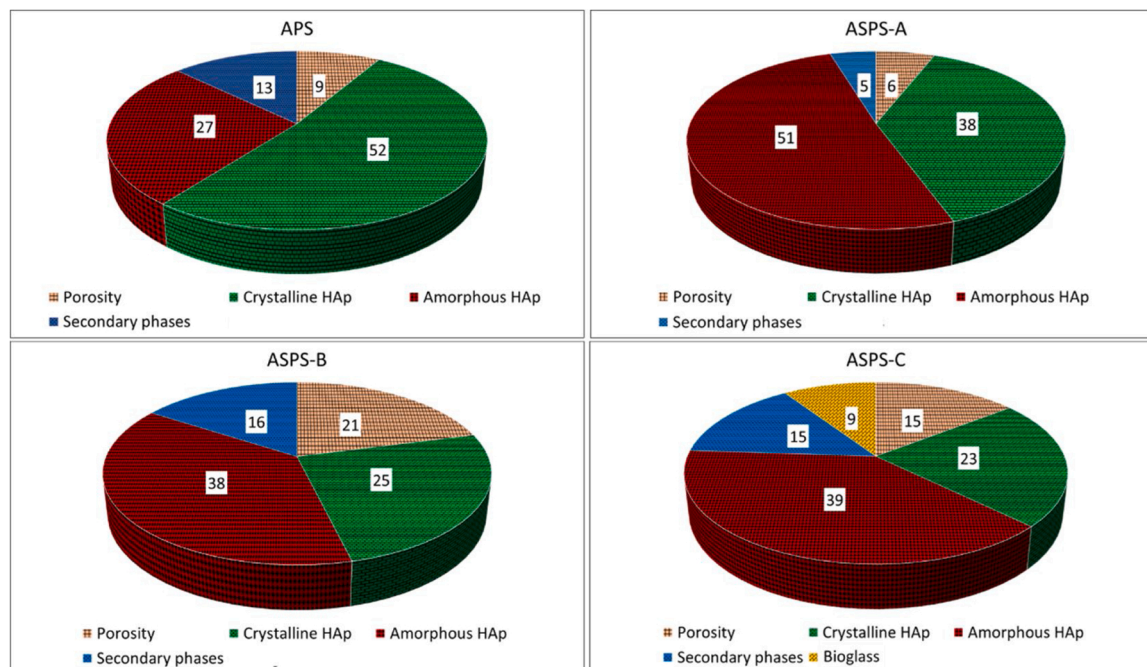

Fig. 7. Relative volume fraction in (%) of various effective coating hardness determining factors such as different phases as well as porosity in different coatings.

phase degradation in different ASPS deposited HAp coatings. The larger the suspension droplet size the lower the amount of heat exchange between the plasma and the HAp powder particles surrounded in a liquid shell. Moreover, larger droplet size gives higher droplet momentum resulting in lower residence time in the plasma plume. As explained in section 3.2 higher solid load content and higher mean solute particle size increases the suspension droplet size.

Among all the three ASPS coatings, ASPS-A coating showed the highest HAp (95 %) phase content (see Fig. 5 (a)), which can be attributed to the reduced heat exchange between the plasma and solute HAp particles due to the larger droplet size of Suspension-A. Moreover, the presence of only about 43 % coating crystallinity rules out the possibility of having scenarios (II, IIA and IV) and suggests that most of the HAp solute particles in Suspension-A followed one or more of the scenarios (I, IA, III or IIIA). Nevertheless, absence of any other phase than HAp (e.g. TTCP or TCP) further narrows down the possibility of the most likely scenarios (III or IIIA). Here about half of each of the HAp particle could have been melted and re-solidified to form an amorphous HAp along with some CaO and hence CaCO$_3$ as explained earlier. Unlike ASPS-A, coating ASPS-B showed about 80 % HAp phase (see Fig. 5) with only 40 % coating crystallinity (see Table 3), which can be attributed to the significantly lower suspension droplet size of Suspension-B than that of Suspension-A. A combination of smaller droplet size, fine initial HAp mean solute particle size, the presence of HAp and Ca(OH)$_2$ phases and the absence of TTCP or TCP phases indicate; that most likely thermal decomposition scenarios for most of the HAp powder particles in ASPS-B coating were either one or a combination of scenarios (II, IIA, III or IIIA). ASPS-C coating showed the least amount of HAp phase content among all. However, the relative decrease i.e. the phase degradation compared to its feedstock was only about 10 %, which is better than ASPS-B (i.e. 20 %) but worse than ASPS-A (i.e. 5%, see Fig. 5). The reason could be the resultant larger droplet size of Suspension-C than that of Suspension-B, but smaller than that of Suspension-A as explained in section 3.2 indicating that the thermal decomposition of most HAp particles in ASPS-C was not as strong as in ASPS-B. Despite of this, the coating crystallinity in ASPS-C was noted to be only 37 % (see Table 3), which is because of the presence of amorphous bio-glass phase in Suspension-C that is also retained in the ASPS-C coating reducing the overall coating crystallinity.

to the requirements set as per the ISO13779−2 standard (i.e., 45 %). As the ASPS technology and its usage for biomedical application is in its very early phase of development, more effort can even minimize such a phase degradation.

3.4. Hardness and adhesion strength of coatings

Hardness and adhesion strengths of all four coatings is presented in Table 3. Hardness in HAp coatings deposited by plasma spray is understood to have a complex dependence on several microstructural features such as porosity and various phases present in the coating [49]. Therefore, in this study, hardness was assumed to be a function of several such variables i.e., porosity, crystalline HAp, amorphous HAp, secondary phases (TCP, TTCP, CaO/other Ca-containing phases) and bioglass. To better understand and compare the hardness of the coatings, a relative volume fraction of all these variables was calculated and shown in Fig. 7 in different pie charts. The relative volume fraction as shown in Fig. 7 was calculated using a rule-of-mixture for porosity and different phases present in the coatings. For example, in case of APS coating, the porosity was about 9% and the rest (i.e., about 91 %) was the bulk which consisted of crystalline HAp, amorphous HAp, secondary phases (e.g., TCP/TTCP/CaO/ other Ca containing phases etc.) and bioglass. The quantification of different phases was done using Rietveld analysis as explained earlier which resulted in 86 % total (crystalline and amorphous) HAp, 0% bioglass and 14 % secondary phases. Moreover, the total coating crystallinity was also calculated separately using Rutland method as per Eq. 1 as explained earlier which resulted in 66 % crystallinity and 34 % total amorphous phase content in the APS coating. However, the total amorphous HAp content was calculated as per Eq. 9 which was about 29 %. Subsequently, the presence of total crystalline HAp content was also calculated as per Eq. 10 which was about 57 %. The relative crystalline HAp content (as reported in Fig. 7) was then calculated using a rule of mixture as per Eq. 11 which was 52 %. Moreover, the relative amorphous HAp phase content was calculated as per Eq. 12, which was 27 %. Similarly, the relative secondary phase content and bioglass content was also calculated which was 13 % and 0%, respectively. Note that the values in bracket in Eqs. 9–12 are for APS coating only.

$$\text{Total amorphous HAp content} = \textit{Total HAp content } (i.e.,\ 86\%) * \frac{\textit{Total amorphous phase content } (i.e.,\ 34\%)}{1000} \tag{9}$$

The likely thermal decomposition scenarios in ASPS-C can be assumed to be similar to ASPS-A due to the larger suspension droplet size and presence of CaCO$_3$ (apart from HAp) i.e. scenarios (III and IIIA). However, significantly lower HAp mean solute particle size also adds the possibility of scenarios (II and IIA) as these fine particles can easily fully melt and re-solidify. Moreover, as discussed earlier in section 3.2, the presence of non-molten region in ASPS-C coating also suggests an additional possibility of scenario (IV).

The discussion on phase degradation of ASPS coatings suggests that although there was phase degradation during plasma spraying of the

$$\text{Total crystalline HAp content} = \textit{Total HAp content } (i.e.,\ 86\%) \\ - \textit{Total amorphous HAp content } (i.e.,\ 29\%) \tag{10}$$

$$\text{Relative cystalline HAp content} = \textit{Bulk content } (91\%) * \frac{\textit{Total crystalline HAp content } (i.e.,\ 57\%)}{100} \tag{11}$$

suspensions, the presence of HAp phase in the coatings was still acceptable and within the limits of requirement stipulated by the FDA (i.e., 80 %). Moreover, the coating crystallinity was also found to be close

Therefore, in the APS coating, predominantly the presence of crystalline HAp (52 %) was noted, followed by an amorphous HAp (27 %) and others balancing the rest i.e., porosity (9%) and secondary phases

$$\text{Relative amorphous HAp content} = \text{Bulk content } (91\%) * \frac{\text{Total amorphous HAp content } (i.e., 29\%)}{100} \qquad (12)$$

(TCP (9%) and CaO (4%)). Therefore, it can be said that the effective coating hardness as reported in Table 3 for APS coating (334 HV) was mostly governed by the presence of crystalline HAp, followed by amorphous HAp and others. It has been shown in the literature that the presence of higher crystalline HAp, lower amorphous HAp and lower porosity in the plasma-sprayed HAp coatings increases the effective coating hardness [49–51]. Moreover, it has been also shown in the literature that the presence of secondary phases such as (TCP/TTCP/CaO/other Ca containing phases) promote the pore filling in the coating ultimately improving the effective hardness of the coating [50]. Therefore, it can be inferred that among all four coatings, the APS coating showed the highest effective coating hardness because of the presence of highest amount of crystalline HAp, lower porosity and relatively high amount of secondary phases.

On the contrary, all ASPS coatings showed greatest contribution of amorphous HAp phase in the total volume fraction compared to other variables. In ASPS-A coating, the amorphous HAp content was highest (51 %), however the presence of lowest porosity (6%) and significantly higher crystalline HAp phase (38 %) than all other ASPS coatings resulted in significantly higher effective coating hardness than other ASPS coatings and about the same hardness as that of the APS coating. Unlike APS and ASPS-A coatings, the balance of volume fraction in both ASPS-B and ASPS-C coatings was uniformly distributed over all the other determining variables. Although, just like in ASPS-A, the presence of amorphous HAp phase content was still the highest among all other variables in both ASPS-B (38 %) and ASPS-C (39 %) coatings. In addition to that, the presence of relatively high porosity in ASPS-B (21 %) and ASPS-C (15 %) coatings resulted in lowest effective coating hardness. A slight increase in the ASPS-C coating's effective hardness compared to ASPS-B coating can be related to the presence of a harder bioglass phase present in the ASPS-C coating.

The hardness results clearly show that by varying the suspension characteristics and thereby the microstructure and phase content of the coatings, it is possible to significantly vary the hardness from as high as 300 HV to as low as 75 HV in suspension-sprayed coatings. As hardness is typically a function of several microstructural features (in this case porosity, crystalline HAp, amorphous HAp, secondary phases and bioglass), tailoring the microstructure in such coatings can allow producing coatings with varying hardness. Compared to APS, ASPS has shown to have a wide process window that allows producing coating microstructures with varying porosity [37]. Although the efforts so far to tailor microstructures and porosity using ASPS technology were focused

mainly on TBC applications, some early efforts in producing hydroxyapatite coatings using SPS [52–54] as well as ASPS [31], technology have already shown the potential to significantly vary the microstructure of such coatings by varying the processing conditions.

Table 3 also reports the adhesion strength of all coatings where the adhesion strength of ASPS-B coating can be observed to be significantly higher than both ASPS coatings (ASPS-A and ASPS-C) as well as the APS coating. The mechanism of adhesion of plasma sprayed HAp coatings with the metallic implants is known to be mechanical interlocking between the splats and the substrate asperities [5]. Therefore, both the substrate roughness or substrate asperities and first few layers of splats on the substrate are crucial factors in governing the coatings adhesion as well as cohesion strength in the vicinity of the substrate-coating interface. As the substrate roughness was identical for all coatings, the governing factor was the splat type (as described in Fig. 6) as well as the size and shape, which were discussed in section 3.2. As explained earlier, all coatings showed a combination of typical pancake-type splats and spherical particles of varied sizes along with non-molten regions. It should be noted that completely molten particle (as shown in Fig. 6 under various thermal decomposition scenarios) in-flight particle has better prospect forming a typical pancake/disc shape splat that flattens on the substrate. The schematic shown in Fig. 8 explains the three possible cases of initial first few layers of splats and substrate asperities interaction depending on the initial feedstock characteristics: (i) assuming that the powder particle/solute particle are completely molten during its in-flight journey (i.e., scenario II from Fig. 6). Deposition of large splats (i.e., splat size >> substrate roughness) as depicted in Case-A can be beneficial for adhesion strength as it can cover several substrate asperities at once and better fill the gaps, which can improve interlocking. However, the high viscosity of the larger molten HAp droplet and their subsequent rapid solidification can still leave the gaps unfilled to some extent. Moreover, the large splats can also introduce large residual stresses at the coating-substrate interface which are detrimental for adhesion strength [5,55]. (ii) However, as depicted in Case-B, the deposition of small splats can not only better fill the gaps to improve the interlocking, but also can minimize the residual stress substantially. (iii) On the contrary, as depicted by Case-C, the deposition of spherical shape re-solidified particles can leave inter-asperity gaps unfilled to a large extent resulting in poor adhesion and weaker cohesion in the vicinity of the substrate coating interface. Also, it must be borne in mind that splats for scenarios other than scenario I from Fig. 6 can also interact in similar way with the substrate asperities as explained above for scenario I, resulting in splats/re-solidified particles/non-molten particles of various size, shapes with different flattening. Based on Fig. 8 and the above discussion, the difference in adhesion strengths of different coatings can be understood as discussed below.

Significantly higher adhesion strength of ASPS-B (42 MPa, see Table 3) coating was due to the formation of predominantly pancake/disc shape, very fine splats and minimum re-solidified spherical particles (see Fig. 2(c1)). This suggests that deposition has followed a combination of Case-B and Case-C (see Fig. 8) with predominantly Case-B type interaction between the splats and the substrate asperities. Moreover, its least coating thickness of ASPS-B (see Table 3) further explains its superior adhesion strength compared to that of other coatings. On the contrary, significantly lower adhesion strength of ASPS-C coating (15 MPa, Table 3) was due to the presence of larger amounts of re-solidified spherical particles (see Fig. 2(d1)), following a combination of Case-B and Case-C with predominantly Case-C type interaction. In addition, Fig. 2 (d1) also shows that most of these re-solidified particles were less
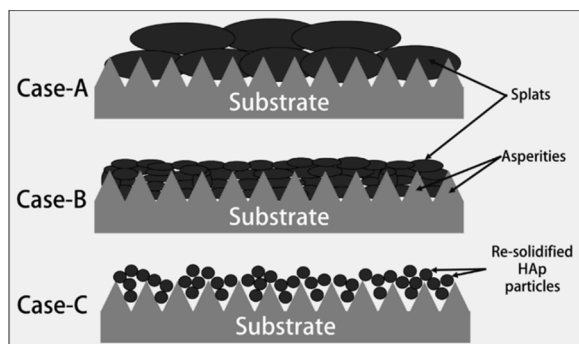

Fig. 8. Three different possible cases of deposition of fully molten HAp particles based on their size and shape on the substrate asperities affecting their adherence to the substrate.

than 3 μm in size, which is less than the average surface roughness of the substrate, further suggesting that the Case-C type interaction was predominantly present in the coating. In addition, the presence of non-molten particles in ASPS-C could have further weakened the adhesion. Moreover, significantly higher coating thickness and the presence of brittle bioglass have further contributed to the reduced adhesion strength of the ASPS-C coating. The presence of bioglass is shown to be detrimental for the adhesion strength of the plasma sprayed HAp coatings due to its brittle nature [56].

In ASPS-A coating, as shown in Fig. 2 (b1) most of the splats formed were significantly bigger than the average surface roughness of the substrate (3 μm) and the presence of spherical shape re-solidified particles were low. This indicates that ASPS-A coating was a combination of all three cases (i.e., Case-A, Case-B and Case-C) with predominantly Case-A type interaction resulting in better adhesion than ASPS-C but still lower than ASPS-B. Similarly, the presence of predominantly large size pancake/disc shape splats in APS coating suggests that the APS coating could have also followed predominantly Case-A type interaction resulting in similar adhesion to ASPS-A. Moreover, higher average splat size and less porosity in both ASPS-A and APS (see Table 3) as well as higher thickness in APS could have introduced higher residual stresses [55] in both coatings, resulting in lower adhesion strength than ASPS-B. The FDA requirement for the adhesion strength of biomedical coatings is more than 50 MPa. Although, this requirement has not been yet met by the coatings as the highest mean adhesion strength observed was just over 40 MPa, a significant improvement in one of the three ASPS deposited coatings compared to the APS coating certainly shows the potential to achieve higher adhesion strength via ASPS if more optimization work is performed on this process.

4. Conclusions and future outlook

This study was aimed to understand the role of feedstock characteristics on microstructure, phase content and mechanical properties of hydroxyapatite (HAp) coatings deposited by an axial plasma spray process with powder as well as suspension feedstock. Use of suspension instead of powder as a feedstock was shown to be beneficial in depositing thinner HAp coatings due to the formation of very fine splats and resultant lower deposition per pass. The lower solid load content and lower mean solute particle size in the suspension was found to be beneficial to achieve porous and rougher coatings due to the formation of spherical particles and nodular features in the coating, respectively. On the contrary, coatings deposited with lower solid load content and lower mean solute particle size suspensions were shown to have higher phase degradation due to the formation of finer suspension droplets, which is beneficial for enhancing the adhesion strength; due to the formation of fine suspension droplets and ensuing higher fine splats along with less re-solidified spherical particles in the coating. In addition, incorporation of bioglass in the feedstock was observed to be deleterious to the adhesion strength of the suspension sprayed HAp coatings due to its brittle nature as well as its tendency to make the HAp suspension more viscous. Successful utilization of the ASPS process to deposit thinner hydroxyapatite coatings with reasonable microstructure and properties opens new possibilities to further explore axial plasma spray for biomedical coating application. Some of the next possible routes moving forward could be the deposition of coatings from suspensions with very low solid load content (<10 wt. %) and nano-sized particle size distribution, deposition of appropriate solution precursor, deposition of composite HAp coatings with the reinforcement of antibacterial agents such as silver, copper etc. or reinforcement with graphene to enhance the mechanical properties etc.

Data availability

The raw/processed data required to reproduce these findings will be made available on request.

CRediT authorship contribution statement

Declaration of Competing Interest

The authors report no declarations of interest.

Acknowledgements

References

[1] K. Søballe, Hydroxyapatite ceramic coating for bone implant fixation, Acta Orthop. Scand. 64 (January (255)) (1993) 1–58, https://doi.org/10.3109/17453679309155636.

[2] K. Rungcharassaeng, J.L. Lozada, J.Y.K. Kan, J.S. Kim, W.V. Campagni, C. A. Munoz, Peri-implant tissue response of immediately loaded, threaded, HA-coated implants: 1-year results, J. Prosthet. Dent. 87 (February (2)) (2002) 173–181, https://doi.org/10.1067/mpr.2002.121111.

[3] J.D. Voigt, M. Mosier, Hydroxyapatite (HA) coating appears to be of benefit for implant durability of tibial components in primary total knee arthroplasty, Acta Orthop. 82 (August (4)) (2011) 448–459, https://doi.org/10.3109/17453674.2011.590762.

[4] C. Courtney, B. Hooks, M.I. Froimson, Hydroxyapatite-coated, tapered titanium hip arthroplasty, Semin. Arthroplasty 20 (March (1)) (2009) 50–54, https://doi.org/10.1053/j.sart.2008.11.006.

[5] R.B. Heimann, Plasma-sprayed hydroxylapatite-based coatings: chemical, mechanical, microstructural, and biomedical properties, J. Therm. Spray Technol. 25 (June (5)) (2016) 827–850, https://doi.org/10.1007/s11666-016-0421-9.

[6] C.-W. Yang, T.-S. Lui, Microstructural self-healing effect of hydrothermal crystallization on bonding strength and failure mechanism of hydroxyapatite coatings, J. Eur. Ceram. Soc. 28 (January (11)) (2008) 2151–2159, https://doi.org/10.1016/j.jeurceramsoc.2008.02.015.

[7] E. Cañas, M. Vicent, E. Bannier, P. Carpio, M.J. Orts, E. Sánchez, Effect of particle size on processing of bioactive glass powder for atmospheric plasma spraying, J. Eur. Ceram. Soc. 36 (February (3)) (2016) 837–845, https://doi.org/10.1016/j.jeurceramsoc.2015.09.039.

[8] V. Cannillo, J. Colmenares-Angulo, L. Lusvarghi, F. Pierli, S. Sampath, In vitro characterisation of plasma-sprayed apatite/wollastonite glass–ceramic biocoatings on titanium alloys, J. Eur. Ceram. Soc. 29 (June (9)) (2009) 1665–1677, https://doi.org/10.1016/j.jeurceramsoc.2008.09.022.

[9] V. Cannillo, L. Lusvarghi, A. Sola, Production and characterization of plasma-sprayed TiO2–hydroxyapatite functionally graded coatings, J. Eur. Ceram. Soc. 28 (January (11)) (2008) 2161–2169, https://doi.org/10.1016/j.jeurceramsoc.2008.02.026.

[10] V. Cannillo, F. Pierli, S. Sampath, C. Siligardi, Thermal and physical characterisation of apatite/wollastonite bioactive glass–ceramics, J. Eur. Ceram. Soc. 29 (March (4)) (2009) 611–619, https://doi.org/10.1016/j.jeurceramsoc.2008.06.034.

[11] ISO 13779-2:2008(en), Implants for Surgery — Hydroxyapatite — Part 2: Coatings of Hydroxyapatite, Accessed: May 03, 2020. [Online]. Available:, International Organization for Standardization, Geneva, Switzerland, 2008 https://www.iso.org/obp/ui/#iso:std:iso:13779:-2:ed-2:v1:en.

[12] B.G. Boe, S.M. Röhrl, T. Heier, F. Snorrason, L. Nordsletten, A prospective randomized study comparing electrochemically deposited hydroxyapatite and

plasma-sprayed hydroxyapatite on titanium stems, Acta Orthop. 82 (February (1)) (2011) 13–19, https://doi.org/10.3109/17453674.2010.548027.

[13] G. Bolelli, et al., Suspension thermal spraying of hydroxyapatite: microstructure and in vitro behaviour, Mater. Sci. Eng. C 34 (January) (2014) 287–303, https://doi.org/10.1016/j.msec.2013.09.017.

[14] R.B. Heimann, Weinheim. Plasma Spray Coating: Principles and Applications, 2nd ed., VCH publishers, 2008.

[15] M.J. Filiaggi, N.A. Coombs, R.M. Pilliar, Characterization of the interface in the plasma-sprayed HA coating/Ti-6Al-4V implant system, J. Biomed. Mater. Res. 25 (October (10)) (1991) 1211–1229, https://doi.org/10.1002/jbm.820251004.

[16] L. Sun, C.C. Berndt, K.A. Gross, A. Kucuk, Material fundamentals and clinical performance of plasma-sprayed hydroxyapatite coatings: a review, J. Biomed. Mater. Res. 58 (5) (2001) 570–592.

[17] C.Y. Yang, B.C. Wang, E. Chang, B.C. Wu, Bond degradation at the plasma-sprayed HA coating/Ti-6Al-4V alloy interface: an in vitro study, J. Mater. Sci. Mater. Med. 6 (May (5)) (1995) 258–265, https://doi.org/10.1007/BF00120268.

[18] R.H. Rothman, W.J. Hozack, A. Ranawat, L. Moriarty, Hydroxyapatite-coated femoral stems. A matched-pair analysis of coated and uncoated implants, JBJS 78 (March (3)) (1996) 319–324, https://doi.org/10.2106/00004623-199603000-00001.

[19] L.D. Dorr, Z. Wan, M. Song, A. Ranawat, Bilateral total hip arthroplasty comparing hydroxyapatite coating to porous-coated fixation, J. Arthroplasty 13 (October (7)) (1998) 729–736, https://doi.org/10.1016/S0883-5403(98)90023-7.

[20] G. Magyar, S. Toksvig-Larsen, A. Moroni, Hydroxyapatite coating of threaded pins enhances fixation, J. Bone Joint Surg. Br. 79 (May (3)) (1997) 487–489, https://doi.org/10.1302/0301-620X.79B3.0790487.

[21] R.B. Heimann, O. Graßmann, H.P. Jennissen, T. Zumbrink, Biomimetic processes during in vitro leaching of plasma-sprayed hydroxyapatite coatings for endoprosthetic applications, Mater. Werkst. 32 (December (12)) (2001) 913–921, https://doi.org/10.1002/1521-4052(200112)32:12<913::AID-MAWE913>3.0.CO;2-H.

[22] G. Bolelli, et al., Comparison between suspension plasma sprayed and high velocity suspension flame sprayed bioactive coatings, Surf. Coat. Technol. 280 (October Supplement C) (2015) 232–249, https://doi.org/10.1016/j.surfcoat.2015.08.039.

[23] L. Pawlowski, Suspension and solution thermal spray coatings, Surf. Coat. Technol. 203 (June (19)) (2009) 2807–2829, https://doi.org/10.1016/j.surfcoat.2009.03.005.

[24] P. Fauchais, G. Montavon, Latest developments in suspension and liquid precursor thermal spraying, J. Therm. Spray Technol. 19 (January (1–2)) (2010) 226–239, https://doi.org/10.1007/s11666-009-9446-7.

[25] F. Tarasi, M. Medraj, A. Dolatabadi, J. Oberste-Berghaus, C. Moreau, Effective parameters in axial injection suspension plasma spray process of alumina-zirconia ceramics, J. Therm. Spray Technol. 17 (November (5–6)) (2008) 685–691, https://doi.org/10.1007/s11666-008-9259-0.

[26] S. Björklund, S. Goel, S. Joshi, Function-dependent coating architectures by hybrid powder-suspension plasma spraying: injector design, processing and concept validation, Mater. Des. 142 (March) (2018) 56–65, https://doi.org/10.1016/j.matdes.2018.01.002.

[27] A. Ganvir, et al., Influence of microstructure on thermal properties of axial suspension plasma-sprayed YSZ thermal barrier coatings, J. Therm. Spray Technol. 25 (November (1–2)) (2015) 202–212, https://doi.org/10.1007/s11666-015-0355-7.

[28] A. Ganvir, N. Curry, S. Bjorklund, N. Markocsan, P. Nylen, Characterization of microstructure and thermal properties of YSZ coatings obtained by axial suspension plasma spraying (ASPS), J. Therm. Spray Technol. 24 (June (7)) (2015) 1195–1204, https://doi.org/10.1007/s11666-015-0263-x.

[29] S. Goel, S. Björklund, N. Curry, U. Wiklund, S. Joshi, Axial suspension plasma spraying of Al2O3 coatings for superior tribological properties, Surf. Coat. Technol. 315 (April Supplement C) (2017) 80–87, https://doi.org/10.1016/j.surfcoat.2017.02.025.

[30] A. Ganvir, V. Vaidhyanathan, N. Markocsan, M. Gupta, Z. Pala, F. Lukac, Failure analysis of thermally cycled columnar thermal barrier coatings produced by high-velocity-air fuel and axial-suspension-plasma spraying: a design perspective, Ceram. Int. (November) (2017), https://doi.org/10.1016/j.ceramint.2017.11.084.

[31] P. Hameed, et al., Axial suspension plasma spraying: an ultimate technique to tailor Ti6Al4V surface with HAp for orthopaedic applications, Colloids Surf. B Biointerfaces 173 (January) (2019) 806–815, https://doi.org/10.1016/j.colsurfb.2018.10.071.

[32] T. Degen, M. Sadki, E. Bron, U. König, G. Nénert, The HighScore suite, Powder Diffr. 29 (December (S2)) (2014) S13–S18, https://doi.org/10.1017/S0885715614000840.

[33] R. Kotian, P.P. Rao, P. Madhyastha, X-ray diffraction analysis of hydroxyapatite-coated in different plasma gas atmosphere on Ti and Ti-6Al-4V, Eur. J. Dent. 11 (4) (2017) 438–446, https://doi.org/10.4103/ejd.ejd_100_17.

[34] T.J. Levingstone, Optimisation of Plasma Sprayed Hydroxyapatite Coatings, Doctoral, Dublin City University, 2008.

[35] Y.C. Tsui, C. Doyle, T.W. Clyne, Plasma sprayed hydroxyapatite coatings on titanium substrates Part 1: mechanical properties and residual stress levels, Biomaterials 19 (November (22)) (1998) 2015–2029, https://doi.org/10.1016/S0142-9612(98)00103-3.

[36] ImageJ Software, Image Processing and Analysis in Java (Accessed 17 November 2014), http://imagej.nih.gov/ij/.

[37] A. Ganvir, S. Joshi, N. Markocsan, R. Vassen, Tailoring columnar microstructure of axial suspension plasma sprayed TBCs for superior thermal shock performance, Mater. Des. 144 (April) (2018) 192–208, https://doi.org/10.1016/j.matdes.2018.02.011.

[38] A. Ganvir, R.F. Calinas, N. Markocsan, N. Curry, S. Joshi, Experimental visualization of microstructure evolution during suspension plasma spraying of thermal barrier coatings, J. Eur. Ceram. Soc. (September) (2018), https://doi.org/10.1016/j.jeurceramsoc.2018.09.023.

[39] A. Ganvir, Design of Suspension Plasma Sprayed Thermal Barrier Coatings, Accessed: May 29, 2018. [Online]. Available:, DIVA, 2018 http://urn.kb.se/resolve?urn=urn:nbn:se:hv:diva-12336.

[40] L. Yan, Y. Leng, L.-T. Weng, Characterization of chemical inhomogeneity in plasma-sprayed hydroxyapatite coatings, Biomaterials 24 (July (15)) (2003) 2585–2592, https://doi.org/10.1016/S0142-9612(03)00061-9.

[41] M. Inagaki, T. Kameyama, Phase transformation of plasma-sprayed hydroxyapatite coating with preferred crystalline orientation, Biomaterials 28 (July (19)) (2007) 2923–2931, https://doi.org/10.1016/j.biomaterials.2007.03.008.

[42] K.A. Gross, C.C. Berndt, P. Stephens, R. Dinnebier, Oxyapatite in hydroxyapatite coatings, J. Mater. Sci. 33 (August (15)) (1998) 3985–3991, https://doi.org/10.1023/A:1004605014652.

[43] S. Dyshlovenko, B. Pateyron, L. Pawlowski, D. Murano, Numerical simulation of hydroxyapatite powder behaviour in plasma jet, Surf. Coat. Technol. 179 (February (1)) (2004) 110–117, https://doi.org/10.1016/S0257-8972(03)00799-0.

[44] M.T. Carayon, J.L. Lacout, Study of the Ca/P atomic ratio of the amorphous phase in plasma-sprayed hydroxyapatite coatings, J. Solid State Chem. 172 (May (2)) (2003) 339–350, https://doi.org/10.1016/S0022-4596(02)00085-3.

[45] R.B. Heimann, Characterization of as-plasma-sprayed and incubated hydroxyapatite coatings with high resolution techniques, Mater. Werkst. 40 (1–2) (2009) 23–30, https://doi.org/10.1002/mawe.200800373.

[46] R.B. Heimann, Thermal spraying of biomaterials, Surf. Coat. Technol. 201 (October (5)) (2006) 2012–2019, https://doi.org/10.1016/j.surfcoat.2006.04.052.

[47] R.B. Heimann, H.D. Lehmann, Bioceramic Coatings for Medical Implants: Trends and Techniques, John Wiley & Sons, 2015.

[48] J. Rolando, T. Candidato, P. Sokołowski, L. Łatka, S. Kozerski, L. Pawłowski, A. Denoirjean, Plasma spraying of hydroxyapatite coatings using powder, suspension and solution feedstocks, Weld. Technol. Rev. 87 (October (10)) (2015), https://doi.org/10.26628/wtr.v87i10.491. Art. no. 10.

[49] L. Sun, C.C. Berndt, C.P. Grey, Phase, structural and microstructural investigations of plasma sprayed hydroxyapatite coatings, Mater. Sci. Eng. A 360 (November (1)) (2003) 70–84, https://doi.org/10.1016/S0921-5093(03)00439-8.

[50] S. Singh, K.K. Pandey, O.S.A. Rahman, S. Haldar, D. Lahiri, A.K. Keshri, Investigation of crystallinity, mechanical properties, fracture toughness and cell proliferation in plasma sprayed graphene nano platelets reinforced hydroxyapatite coating, Mater. Res. Express 7 (January (1)) (2020) 015415, https://doi.org/10.1088/2053-1591/ab6c23.

[51] A. Mejias, R.T. Candidato, L. Pawłowski, D. Chicota, Mechanical properties by instrumented indentation of solution precursor plasma sprayed hydroxyapatite coatings: analysis of microstructural effect - ScienceDirect, Surf. Coat. Technol. 298 (July) (2016) 93–102, https://doi.org/10.1016/j.surfcoat.2016.04.028.

[52] J. Cizek, et al., Silver-doped hydroxyapatite coatings deposited by suspension plasma spraying, J. Therm. Spray Technol. 27 (December (8)) (2018) 1333–1343, https://doi.org/10.1007/s11666-018-0767-2.

[53] Y. Bai, B. Chi, W. Ma, C. Liu, Suspension plasma-sprayed fluoridated hydroxyapatite coatings: effects of spraying power on microstructure, chemical stability and antibacterial activity, Surf. Coat. Technol. 361 (March) (2019) 222–230, https://doi.org/10.1016/j.surfcoat.2019.01.051.

[54] I. Ročňáková, et al., Deposition of hydroxyapatite and tricalcium phosphate coatings by suspension plasma spraying: effects of torch speed, J. Eur. Ceram. Soc. 38 (December (16)) (2018) 5489–5496, https://doi.org/10.1016/j.jeurceramsoc.2018.08.007.

[55] L. Gu, et al., Influence of ceramic thickness on residual stress and bonding strength for plasma sprayed duplex thermal barrier coating on aluminum alloy, Surf. Coat. Technol. 206 (June (21)) (2012) 4403–4410, https://doi.org/10.1016/j.surfcoat.2012.04.070.

[56] L. Altomare, et al., Microstructure and in vitro behaviour of 45S5 bioglass coatings deposited by high velocity suspension flame spraying (HVSFS), J. Mater. Sci. Mater. Med. 22 (May (5)) (2011) 1303, https://doi.org/10.1007/s10856-011-4307-6.